catalysts

MDPI

Article

The Influence of Precursor on the Preparation of CeO_2 Catalysts for the Total Oxidation of the Volatile Organic Compound Propane

Kieran Aggett, Thomas E. Davies, David J. Morgan, Dan Hewes and Stuart H. Taylor *

Cardiff Catalysis Institute, School of Chemistry, Cardiff University, Main Building, Park Place, Cardiff CF10 3AT, UK; aggettk@cardiff.ac.uk (K.A.); DaviesTS@cardiff.ac.uk (T.E.D.); morgandj3@cardiff.ac.uk (D.J.M.); hewesdg@cardiff.ac.uk (D.H.)
* Correspondence: taylorsh@cardiff.ac.uk; Tel.: +44-(0)29-2087-4062

Abstract: CeO_2 catalysts were prepared by a precipitation method using either $(NH_4)_2Ce(NO_3)_6$ or $Ce(NO_3)_3$, as Ce^{IV} or Ce^{III} precursors respectively. The influence of the different precursors on catalytic activity was evaluated for the total oxidation of propane with water present in the feed. The catalyst prepared using the Ce^{IV} precursor was more active for propane total oxidation. The choice of precursor influenced catalyst properties such as surface area, reducibility, morphology, and active oxygen species. The predominant factor associated with the catalytic activity was related to the formation of either $CeO_2.nH_2O$ or $Ce_2(OH)_2(CO_3)_2.H_2O$ precipitate species, formed prior to calcination. The formation of $CeO_2.nH_2O$ resulted in enhanced surface area which was an important factor for controlling catalyst activity.

Keywords: VOC total oxidation; cerium oxide; propane oxidation; cerium precursor

Citation: Aggett, K.; Davies, T.E.; Morgan, D.J.; Hewes, D.; Taylor, S.H. The Influence of Precursor on the Preparation of CeO_2 Catalysts for the Total Oxidation of the Volatile Organic Compound Propane. *Catalysts* **2021**, *11*, 1461. https://doi.org/10.3390/catal11121461

Academic Editor: Renaud Cousin

Received: 6 November 2021
Accepted: 22 November 2021
Published: 30 November 2021

1. Introduction

Volatile organic compounds (VOCs) are associated with various issues affecting the environment and human health [1]. For example, the formation of ground level ozone from the reaction of VOCs with NO_x species in the atmosphere has been linked with respiratory issues in humans, as well as some VOCs being known carcinogens [2]. VOCs are wide ranging in their chemical nature and short chain alkanes, such as propane, are known to be difficult to remove from the atmosphere [3], hence propane is an excellent model compound to study. In addition, the increasing use of liquid petroleum gas (LPG) as a transport fuel has led to a rise in propane emissions [4]. As short chain alkane emissions are linked to mobile and stationary sources including the petroleum industry and vehicle exhausts, other compounds such as water vapour may co-exist in the gas feed [5]. These compounds are thought to affect the removal of VOCs such as propane, therefore recent research has also focused on the impact of the conditions used for VOC removal [6,7].

Control of VOC emissions is of growing concern and mitigation can be achieved in many ways, such as thermal oxidation, catalytic oxidation, adsorption, and absorption [8,9]. However, catalytic oxidation has been identified as a more efficient way to remove VOCs, requiring less energy than thermal oxidation, and unlike adsorption and absorption techniques it is a destructive process. Catalytic oxidation also has the ability to simultaneously remove multiple VOCs from waste streams and treat low levels of VOCs [10]. In addition, catalytic oxidation has the benefit of producing more environmentally benign products in comparison with toxic by-products often created by thermal oxidation [11]. Noble metal catalysts containing Pd and Pt have been widely reported as active catalysts for VOC oxidation; however, there is a driving force to switch to metal oxide catalysts, as they have the advantage of being less expensive and more abundant [12].

Amongst the metal oxide catalysts reported, cerium (IV) oxide (CeO_2) is widely regarded as an effective oxidation catalyst, due to many beneficial characteristics. The

favourable redox properties of CeO_2, in addition to its high oxygen storage capacity (OSC), and ability to form oxygen defects, which enable fast oxygen mobility through the lattice, has made it the catalyst of choice for various oxidation reactions [13–16]. Furthermore, many other metal oxides have been used in conjunction with CeO_2 to enhance their characteristics, resulting in more active catalysts for soot [17] and benzene [18] oxidation. The morphology of CeO_2 based catalysts can also be finely tuned to selectively control the exposed facets. This method has been employed for a range of oxidation reactions, leading to surface interactions improving catalytic activity [19–21]. The impact of adsorbed species, such as water vapour, on different CeO_2 surfaces has also been studied in the literature [22] which is important when considering reaction conditions used. The structure and transformation of cerium precursors to form CeO_2 have been studied, leading to materials with varying characteristics, but few consider the catalytic uses for these materials [23]. Recent research on the influence of the cerium precursor salt for catalysts have mainly been studied in the context of mixed metal oxides [24–26], but single oxide CeO_2 has rarely been investigated.

It is well established that altering the synthesis route for catalyst preparation can drastically influence the activity trends for various reactions [27]. Altering preparation method, aging and calcination conditions have all been shown to result in varied catalyst characteristics, which can improve activity [14]. For example, precipitation allows for the careful control of synthesis parameters such as pH, aging time, solution concentrations and precipitating agent. However, the influence of the metal precursor can sometimes be overlooked.

In this work, two CeO_2 catalysts were prepared by a precipitation method, using either $(NH_4)_2Ce(NO_3)_6$ or $Ce(NO_3)_3$ as the precursor cerium source. These catalysts were characterised by X-ray diffraction (XRD), X-ray photoelectron spectroscopy (XPS), Thermal gravimetric analysis-Differential thermal analysis (TGA-DTA), Laser Raman spectroscopy, Temperature programmed reduction (TPR), Electron microscopy (TEM/SEM), and Brunauer–Emmett–Teller (BET) surface area analysis. Catalysts were evaluated for the total oxidation of propane as a model VOC, focusing on the impact the cerium precursor had on the catalytic activity and how it can be related to the structure, redox properties, and surface state of the CeO_2 catalysts.

2. Results and Discussion

2.1. Catalyst Precursor Characterisation

The dried catalyst precursors prior to calcination were analysed using powder XRD (Figure 1) and there was a significant difference between the two precipitated precursors. The d-CeO_2 (IV) sample had a structure representative of a cubic CeO_2 phase with low crystallinity, exhibiting reflections at 29°, 33°, 47°, and 57°, corresponding to (111), (200), (220) and (311) lattice planes, respectively. Whereas the d-CeO_2 (III) sample predominantly exhibited reflections representing an orthorhombic $Ce_2(OH)_2(CO_3)_2.H_2O$ structure [28], with other additional reflections identified as hexagonal $Ce(OH)(CO_3)$. Hence, under these synthesis conditions, the Ce^{IV} and Ce^{III} precursors follow two different chemical precipitation mechanisms.

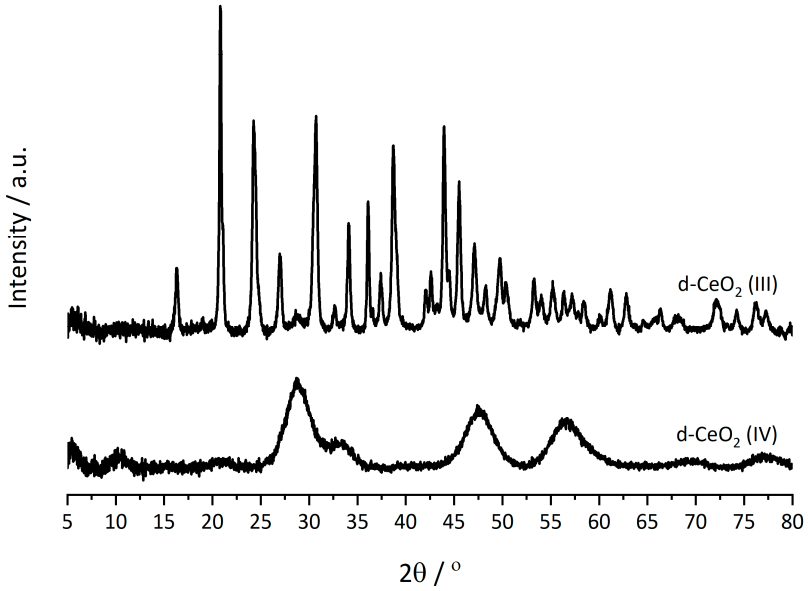

Figure 1. Powder X-ray diffraction patterns of precipitated catalyst precursors prior to calcination.

Thermal decomposition of the precipitated catalyst precursors were analysed using TGA-DTA (Figure 2a,b). Around 7% mass loss was observed from the d-CeO_2 (IV) sample over the range 100–500 °C. In contrast, the d-CeO_2 (III) sample showed a mass loss of 23% with a small decrease around 70 °C, followed by a sharp decrease between 250–300 °C. These were associated with the evolution of H_2O species and decomposition of carbonate species from the dried sample respectively; confirming that the precipitate formed from the Ce^{III} precursor was a $Ce(CO_3)_x(OH)_y$ type species [29]. Furthermore, the endothermic peak around 250 °C, characterised by DTA, is attributed to the liberation of CO_2 from the decomposition of carbonate species [30]. The broad endothermic peak observed between 50–250 °C, in the d-CeO_2 (IV) sample, can be attributed to the evolution of H_2O. Previous work carried out by Hirano et al. looked at the precipitation mechanism of different Ce^{IV} and Ce^{III} precursors using urea prepared by hydrothermal synthesis [31,32]. They discovered that when using a Ce^{IV} precursor, hydrated $[Ce(OH)_y(H_2O)_{n-y}]^{(4-y)+}$ ions were formed as a result of the ability to undergo strong hydration from the lower basicity and higher charge of the Ce^{4+} ion. This caused $CeO_2.nH_2O$ to precipitate rapidly before reaction with carbonate to form $Ce(CO_3)_x(OH)_y$ type species could occur. Evidence of CeO_2 nanoparticle formation from the hydrolysis of ammonium cerium nitrate in aqueous solution without the addition of a base has also been documented by Pettinger et al. [33]. This effect was not observed when using different Ce^{III} precursors, and the products formed were the carbonates, either $Ce_2O(CO_3)_2.H_2O$ or $Ce(OH)CO_3$ [31].

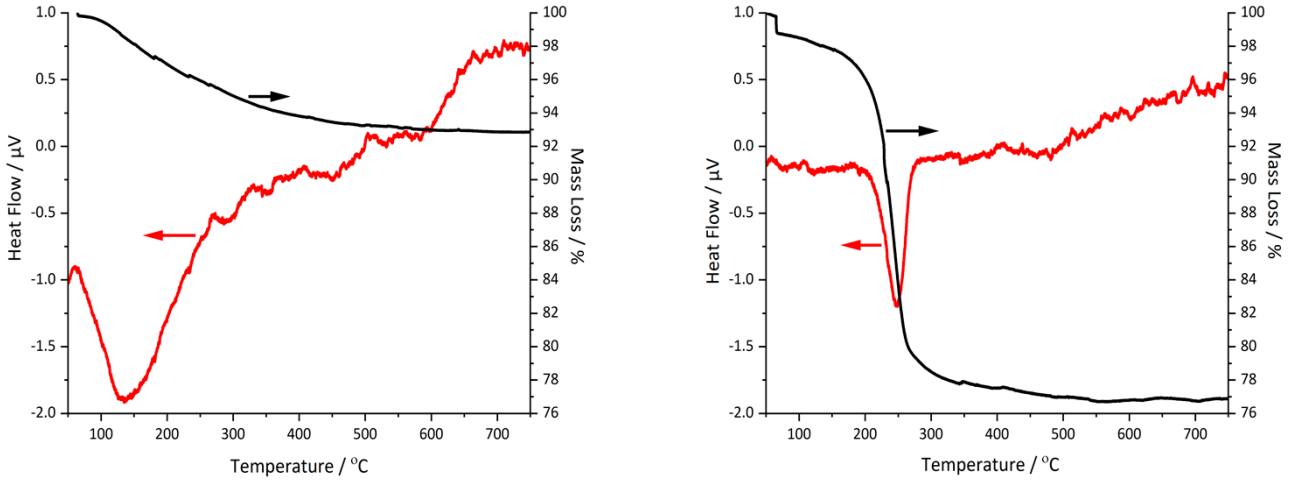

Figure 2. Thermal gravimetric and differential thermal analysis of the precipitated catalyst precursors: (**a**) d-CeO_2 (IV) and (**b**) d-CeO_2 (III). Samples heated under flowing air atmosphere from 50 to 750 °C at 5 °C min^{-1}.

Based on the bulk phases identified from XRD, the theoretical mass losses were calculated for each thermal decomposition, assuming CeO_2 was the final product.

$$Ce_2(OH)_2(CO_3)_2.H_2O \rightarrow 2CeO_2 \quad (1)$$

$$CeO_2.nH_2O \rightarrow CeO_2 \quad (2)$$

For the Ce^{III} precursor, the theoretical mass loss was calculated to be 24% which is in good agreement with the 23% experimental loss identified by TGA-DTA analysis. From the XRD data, the formation of hydrated CeO_2 particles in solution was the only product formed using the Ce^{IV} precursor. Therefore, a mass loss of 7% equates to 0.67 H_2O.

2.2. Catalyst Characterisation

Table 1 summarises some of the characterisation data for the two CeO_2 catalysts. The BET surface areas were significantly different for the two catalysts, with CeO_2 (IV) having a surface area roughly four times larger than CeO_2 (III). The adsorption–desorption isotherms for the two catalysts differ (Figure 3a,b), indicating diverse pore structures. Both plots represent a type IV isotherm, indicative of a mesoporous-type structure, with the CeO_2 (IV) catalyst having an H2 hysteresis loop. This type of hysteresis is indicative of capillary condensation in disordered and ill-defined pore structures, suggesting a higher porosity, which would be consistent with the higher surface area shown for this catalyst. In contrast, the CeO_2 (III) catalyst shows an H3 hysteresis loop, which is related to the formation of non-rigid, plate-like particles that form a disordered pore structure with slit-shaped pores [34]. In addition, hysteresis of this kind is linked with the incomplete filling of macropores, suggesting a higher concentration of macropores in this catalyst [35].

Table 1. Physiochemical properties of CeO_2 (IV) and CeO_2 (III) catalysts calcined at 500 °C for 3 h in static air.

Catalyst	Surface Area/m^2 g^{-1}	Average Crystallite Size/nm	Lattice Parameter/nm	A_{590}/A_{463}
CeO_2 (IV)	81	8.7	0.5409	0.018
CeO_2 (III)	19	9.3	0.5408	0.019

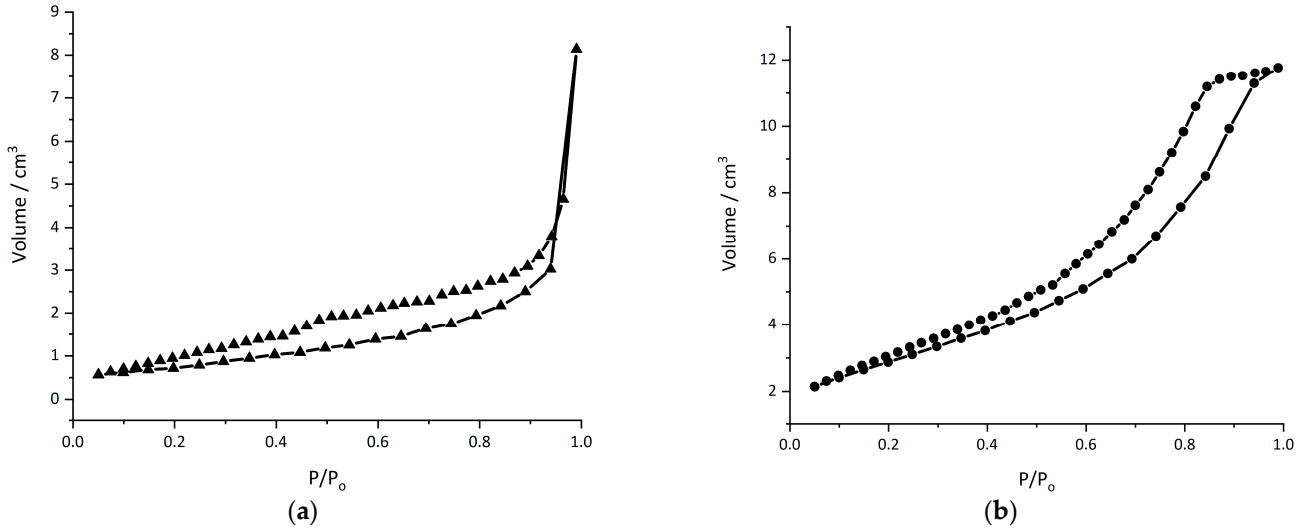

Figure 3. N_2 Adsorption–desorption isotherms of (**a**) CeO2 (IV) and (**b**) CeO2 (III) catalysts.

SEM images shown in Figure 4 indicate the different morphologies of the catalysts. This information helps to rationalise the surface area and adsorption–desorption isotherm data previously discussed. The CeO_2 (III) catalyst displays clumped aggregates with platelet or needle-like structures, which is representative of the H3 hysteresis loop; whereas, the CeO_2 (IV) catalyst forms larger well-defined particles. From the characterisation of the precipitates formed during the synthesis, it can be suggested that the presence of the $Ce_2(OH)_2(CO_3)_2.H_2O$ phase ensures the formation of these type of non-rigid aggregates seen for CeO_2 (III). In contrast, forming the $CeO_2.nH_2O$ precipitate forms the well-defined structures shown for CeO_2 (IV).

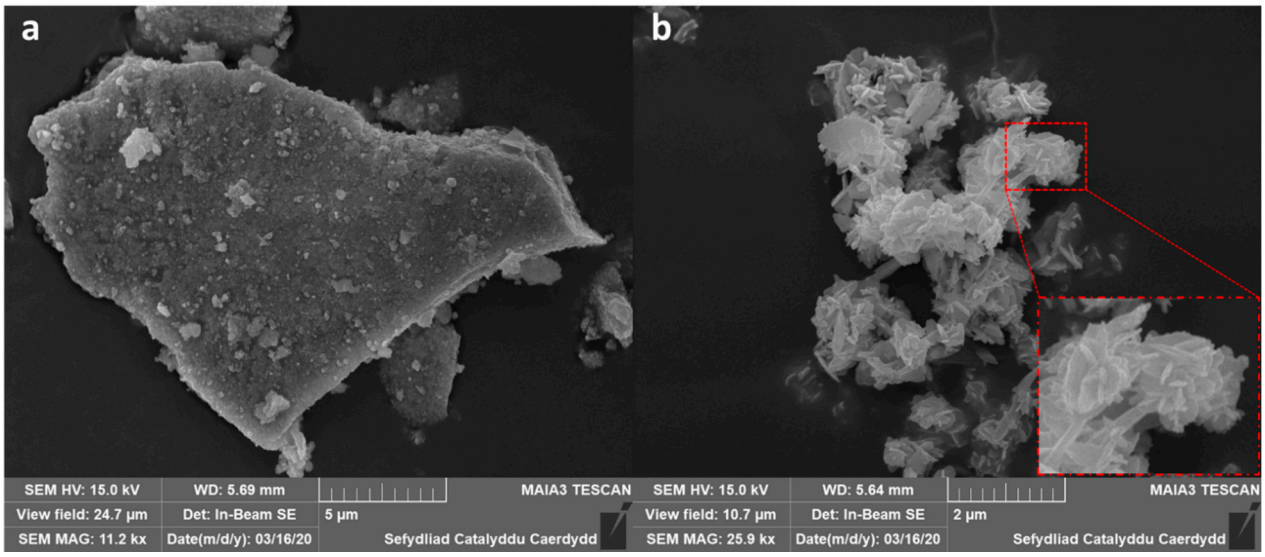

Figure 4. Scanning electron microscopy images of (**a**) CeO_2 (IV) and (**b**) CeO_2 (III) catalysts. Inset shows platelet type morphology.

TEM images displayed in Figure 5 strengthen conclusions drawn from the SEM data. Differences in large scale morphology are apparent between CeO_2 (IV) and CeO_2 (III) (Figure 5a,d). However, the small-scale morphology appears similar (Figure 5b,e), with both CeO_2 (IV) and CeO_2 (III) samples showing agglomerated, small facetted CeO_2 particles of 8–10 nm, consistent with the crystallite size determined by XRD. High magnification images representative of the catalyst samples (Figure 5c,f) were used to measure the interplanar distances present on the CeO_2 (IV) and CeO_2 (III) catalysts, which could be noticed in

different regions (Figure 5b,e). The interplanar distances were 0.31 nm for both samples which is representative of the (111) lattice planes, indicating their preferential exposure.

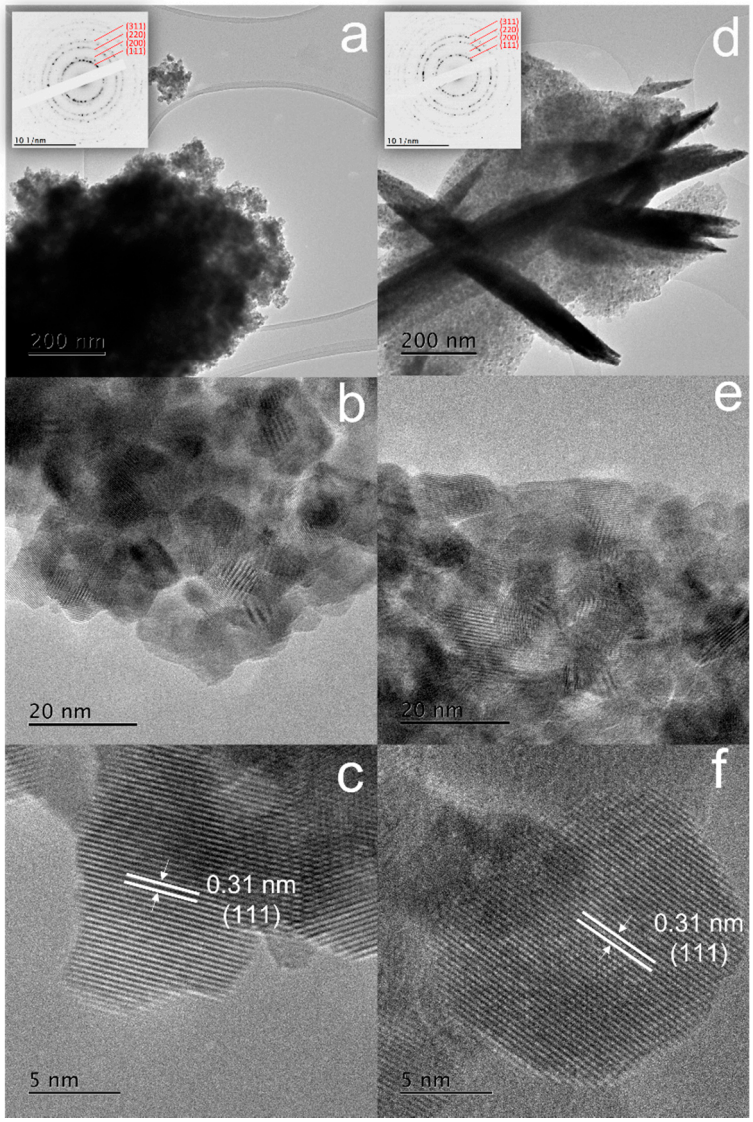

Figure 5. Transmission electron microscopy images and selected area electron diffraction patterns of (**a**–**c**) CeO_2 (IV) and (**d**–**f**) CeO_2 (III) catalysts.

Data acquired from XRD analysis of the two catalysts shown in Figure 6 indicates a similar bulk structure. XRD patterns of the catalysts only showed the cubic fluorite structure of CeO_2, with the lattice parameters of both catalysts within 0.0001 nm of each other. This is also consistent with the structure identified by selected area electron diffraction (SAED) analysis (Figure 5a,d). The crystallite sizes were calculated using the Scherrer equation by taking an average of the values obtained when analysing the peak widths of the four dominant (111), (200), (220), and (311) reflections. The sizes calculated were similar for both catalysts, with the CeO_2 (IV) catalyst having a slightly smaller crystallite size on average (8.7 nm verses 9.3 nm, Table 1). However, the average crystallite sizes calculated are within the experimental error ($\pm$1.2 nm), hence no significant difference can be identified.

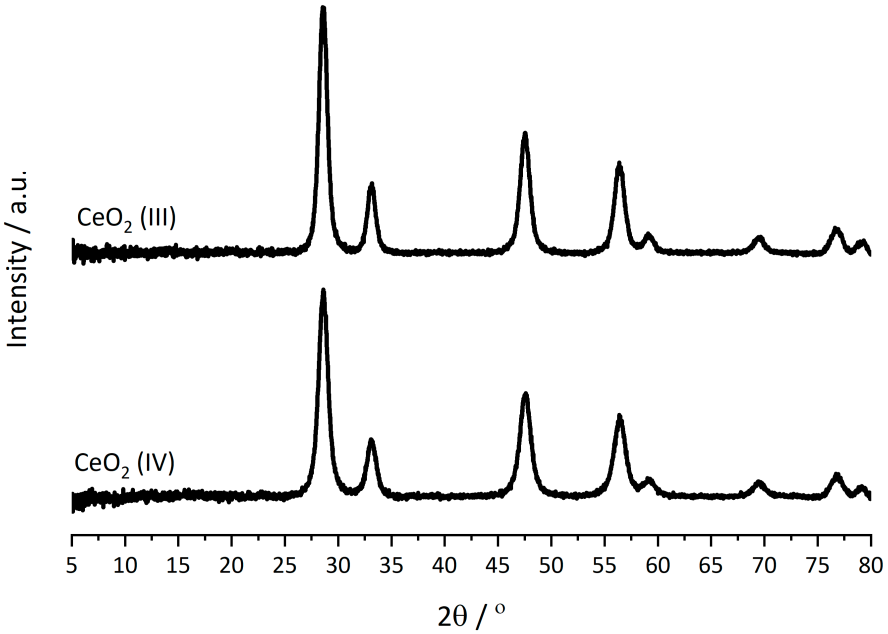

Figure 6. Powder X-ray diffraction patterns of the CeO_2 catalysts.

It is well established that CeO_2 catalysts exhibit an intense Raman band around 460 cm^{-1}, relating to the F_{2g} vibrational mode. Other weaker bands are active, such as a band around 600 cm^{-1}, which is associated with the presence of defect sites [36]. It has been previously established that the ratio of these two peaks can be used to estimate the concentration of defect sites in the material, which can then be used to greater understand the redox properties and oxygen mobility through the lattice of these types of catalysts [37]. This factor is especially important for propane total oxidation as it is thought that it takes place via a Mars-van Krevelen mechanism [12]. The Raman spectra shown in Figure 7 matches that of the cubic fluorite CeO_2 structure, consistent with that determined by XRD. The intense band at 463 cm^{-1} denotes the F_{2g} vibrational mode, and a small band around 590 cm^{-1} indicated the presence of some defect species. The ratio of bands at 590 cm^{-1} and 463 cm^{-1} (A_{590}/A_{463}) are shown in Table 1, and they are very similar for both catalysts, which implies that the defect concentrations of both catalysts detectable by Laser Raman spectroscopy are similar.

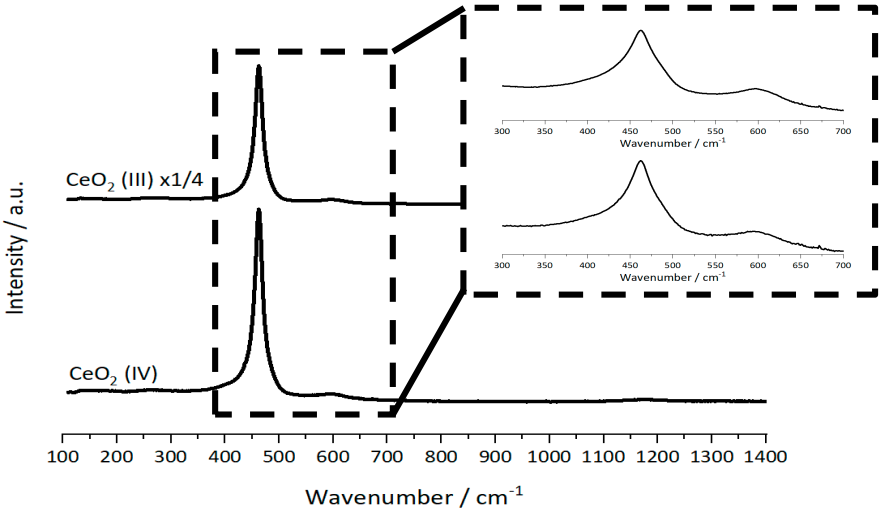

Figure 7. Laser Raman Spectra of the CeO_2 catalysts. Inset shows band relating to defects.

From the TPR profiles shown in Figure 8, only one main reduction peak was observed for both catalysts. This peak occurred at similar temperatures for both catalysts, 478 °C for CeO_2 (III) and 498 °C for CeO_2 (IV). CeO_2 has two main types of reduction features, these are the reduction of surface species and the reduction of bulk lattice species [38]. Bulk reduction occurs at temperatures above 700 °C, whilst surface reduction occurs around 500 °C, therefore, the features present in the TPR profiles relate to the reduction and removal of oxygen species from the catalyst surface. Table 2 shows the H_2 consumption normalised for surface area and mass for both catalysts. Both catalysts exhibit good redox ability; however, the CeO_2 (III) catalyst had a higher H_2 consumption normalised for surface area. This factor, in combination with the lower temperature peak for the surface reduction, suggests CeO_2 (III) had a greater extent of surface reduction, and that reduction was slightly more facile compared to CeO_2 (IV). These differences between CeO_2 (III) and CeO_2 (IV), could possibly arise as a result of different structures, identified by SEM, originating from the different synthesis precursors and the subsequent transformation into the CeO_2 catalysts.

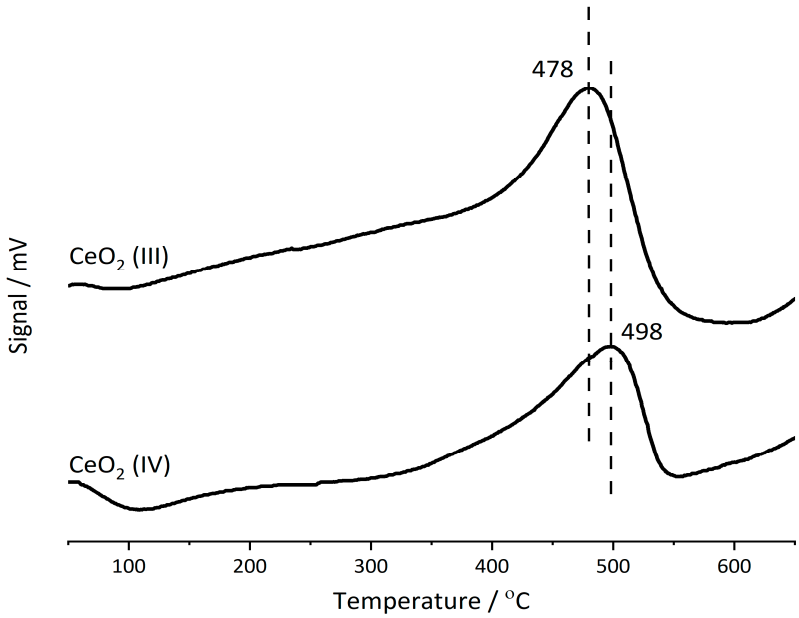

Figure 8. Temperature programmed reduction profiles of CeO_2 (IV) and CeO_2 (III) catalysts. Conditions: 10% H_2/Ar, 30 mL min^{-1}, 50–700 °C at 10 °C min^{-1}.

Table 2. H_2 Consumption of CeO_2 (IV) and CeO_2 (III) catalysts determined from temperature programmed reduction.

Catalyst	TPR Cycle	H_2 Consumption Per Surface Area/μmol m^{-2}	H_2 Consumption Per Mass/μmol g^{-1}
CeO_2 (IV)	1	0.435	35.20
	2	0.145	11.73
CeO_2 (III)	1	4.575	86.93
	2	0.464	8.81

To assess oxygen storage capacity (OSC), TPR-TPO cycles were performed. Data in Table 2 affirms the trend shown in the TPR analysis, with CeO_2 (III) having a higher H_2 consumption than the CeO_2 (IV) catalyst. However, upon re-oxidising and then reducing the catalysts again, the H_2 consumption for the CeO_2 (III) catalyst decreased significantly. The results for the H_2 consumption per surface area indicated a decrease by a factor of 10 for the CeO_2 (III) catalyst, whilst the decrease was only three-fold for the CeO_2 (IV), bringing the values closer together for both catalysts. This analysis also suggests that the

first TPR analysis may not be representative of the redox properties of the catalyst under reaction conditions. Furthermore, it has been suggested that the re-oxidation of the catalyst is the rate determining factor [38], hence there may not be a direct relationship between propane oxidation activity and H_2 consumption.

Core-level Ce 3d photoelectron spectra for both CeO_2 (III) and (IV) catalysts are shown in Figure 9. Given the large number of final states arising from photoemission, Ce 3d XPS spectra are recognised as being difficult to analyse; however, it is generally accepted a total of 10 peaks are present for CeO_2 relating to mixed (III)/(IV) states. These peaks are divided into the Ce^{3+} and Ce^{4+} oxidation states with peaks denoted v_0, v′, u_0, u′ being used to calculate the concentration of Ce^{3+} and v, v″, v‴, u, u″, u‴ used to represent the Ce^{4+} oxidation state [39]. The ratio of surface Ce^{3+} to Ce^{4+} was calculated using the integrated peak areas of each relative fitting of the two oxidation states (Table 3). The CeO_2 (IV) catalyst shows a higher ratio, indicating a higher concentration of reduced Ce^{3+} species, which is initially counterintuitive using a precursor with cerium in the +4 oxidation state. It is proposed that the higher concentration of Ce^{3+} surface species directly relates to an increased amount of surface defect sites, which can affect catalytic activity [21,37,38,40]. The increased amounts of reduced Ce^{3+} surface species in the CeO_2 (IV) catalyst can also be linked to the lower surface H_2 consumption determined by TPR analysis. The lower quantity of reduction, defined by H_2 consumption, for the CeO_2 (IV) catalyst could be a direct result of the higher concentration of Ce^{3+} species identified, hence the CeO_2 (IV) catalyst would initially have a more reduced surface.

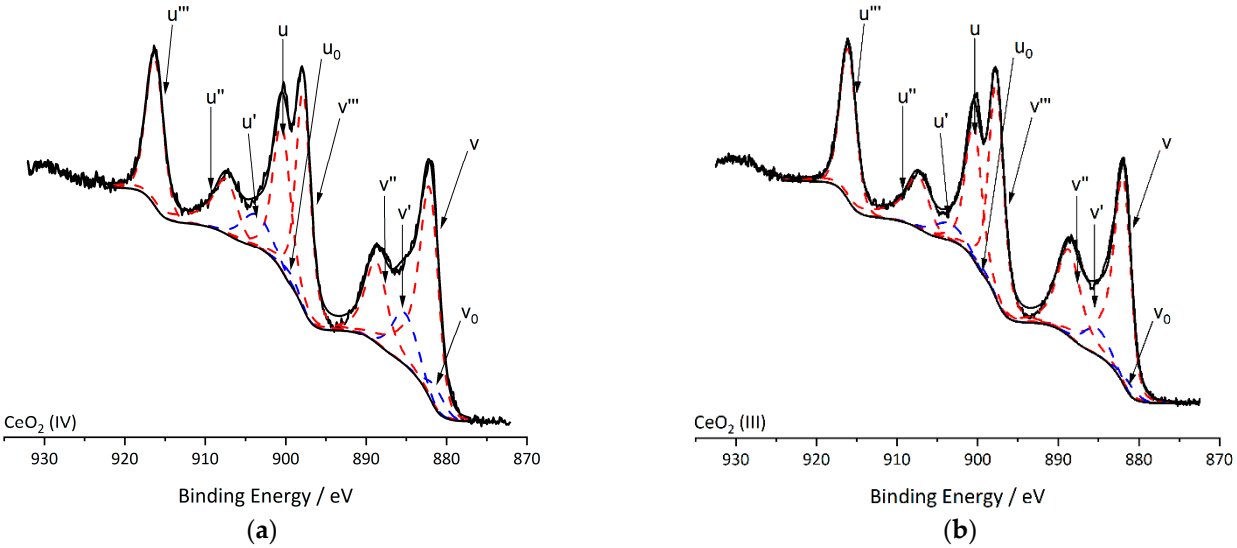

Figure 9. X-ray photoelectron spectra of Ce 3d region for (**a**) CeO_2 (IV) and (**b**) CeO_2 (III) catalysts, where fitted peaks refer to Ce^{3+} (blue) and Ce^{4+} (red) states.

Table 3. X-ray photoelectron spectroscopy and energy dispersive X-ray analysis derived surface elemental composition for the CeO_2 catalysts.

Catalyst	XPS Ce:O:Na Ratio	O^{β}/O^{α} Ratio	Ce^{3+}/Ce^{4+} Ratio	EDX Ce:O:Na Ratio
CeO_2 (IV)	29:68:3	0.438	0.155	30:68:2
CeO_2 (III)	22:67:11	0.289	0.086	34:59:7

Catalytic activity may also be influenced by the surface oxygen species. Figure 10 shows the fitted O 1s core-level spectra for both catalysts. Two distinct oxygen species/environments can be extracted from the spectra, which we ascribe as O^{β} (531 eV) and O^{α} (529 eV) states, reported to be characteristic of defect oxygen and lattice oxygen species respectively [37,41]. There is some controversy on the labelling of the O^{β} region; it is thought that this region could also relate to the presence of hydroxyl and carbonate

oxygen species [37]. However, some researchers have linked it to the appearance of low co-ordination oxide ions [41,42]. As a result, the species represented by the O^{β} region have been referred to as surface oxygen defect sites. The ratio of O^{β}/O^{α} shown in Table 3 indicates the CeO_2 (IV) catalyst has a higher proportion of surface oxygen defect sites compared to the CeO_2 (III) catalyst, which is self-consistent with the higher quantity of Ce^{3+} on the surface determined by XPS analysis of the Ce 3d region. In contrast, data acquired by Laser Raman spectroscopy showed little difference in defect concentration between the catalysts and suggests the defects are highly localised in the near surface region, due to the surface sensitivity of XPS, and the bulk sampling of Laser Raman.

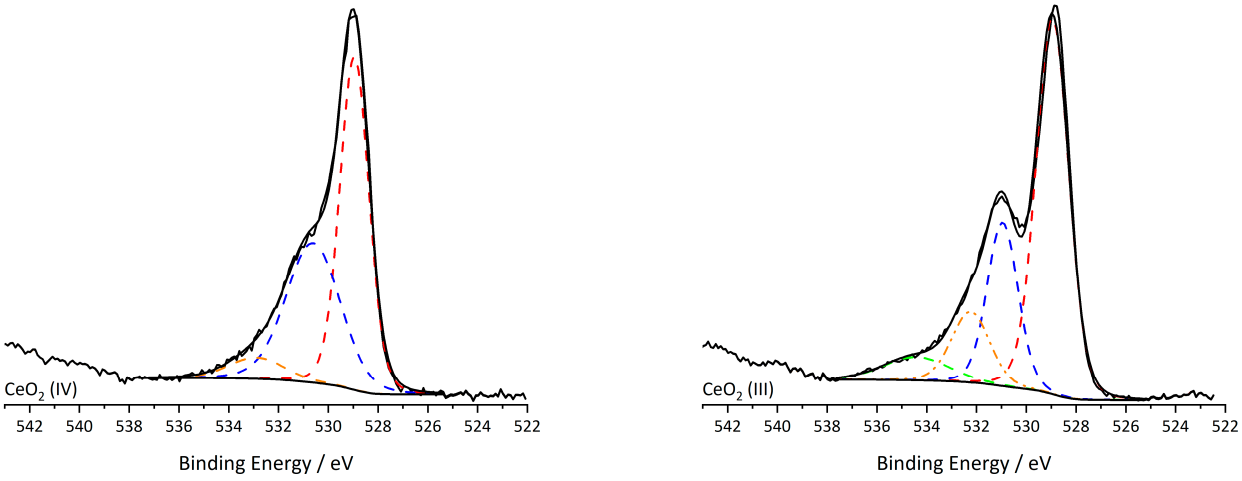

Figure 10. X-ray photoelectron spectra of O 1s peaks for calcined (**a**) CeO_2 (IV) and (**b**) CeO_2 (III) catalysts, where fitting shows the O^{α} (red), O^{β} (blue) oxygen species as described in the main text and yellow and green refer to the overlapping Na Auger peaks.

In addition to using XPS to identify surface oxygen and cerium species, it is also important to look at other surface species that could be present, which could affect catalytic activity. Alkali metals, such as Na, present from precipitation using Na_2CO_3, have been proposed as a catalyst poison for certain oxidation reactions by metal oxides [43]. From the XPS data shown in Table 3, the surface content of Na is much higher on CeO_2 (III) compared with CeO_2 (IV). This can also be evidenced from the presence of the Na Auger signal (green curve, Figure 10) in the O 1s spectra for CeO_2 (III). This effect is consistent with the EDX data, which shows that the CeO_2 (III) catalyst also has a higher bulk Na content (Table 3). As both catalyst precursors underwent the same extensive washing procedure, the precursor carbonate phase of the CeO_2 (III) appears to be more efficient in retaining Na.

2.3. Catalyst Performance

Catalyst performance for propane total oxidation is shown in Figure 11 for CeO_2 (IV) and CeO_2 (III) catalysts. The main reaction product detected was CO_2 and both catalysts maintained a carbon balance of >98%. Selectivity to CO_2 was >99% across the temperature range for CeO_2 (IV), whilst between 500–600 °C it was 96% for CeO_2 (III), due to the formation of low levels of propene. It is clear that the CeO_2 (IV) catalyst was more active for propane total oxidation across the temperature range. Data shown in Table 4 indicates that, when normalised for surface area, both catalysts had similar activity for propane oxidation.

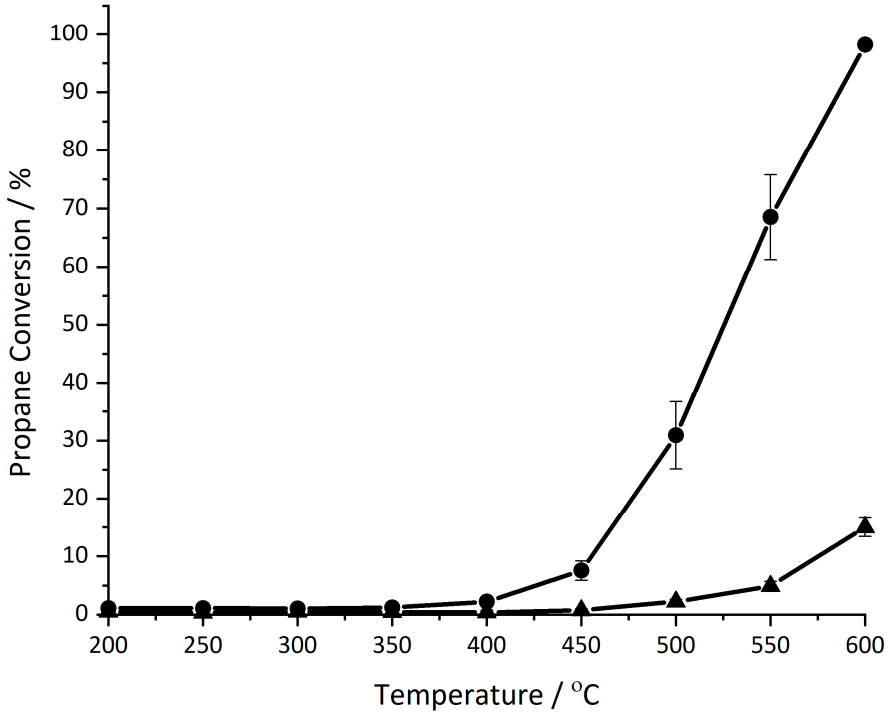

Figure 11. Catalyst activity for propane total oxidation in the presence of water vapour: (Circle) CeO_2 (IV) and (Triangle) CeO_2 (III). Conditions: 5000 ppm propane in air, GHSV = 45,000 h^{-1}, 5% Water Saturation.

Table 4. Mass normalised and surface area normalised catalytic activity of CeO_2 (IV) and CeO_2 (III) catalysts for propane total oxidation.

Catalyst	Propane Conversion/%	Surface Area Normalised Propane Oxidation [a]/mol s^{-1} m^{-2}	Mass Normalised Propane Oxidation [a]/mol s^{-1} g^{-1}
CeO_2 (IV)	50	3.73×10^{-3}	3.02×10^{-1}
CeO_2 (III)	4	3.68×10^{-3}	6.99×10^{-2}

[a] Calculated at 525 °C.

A comparison between wet and dry conditions, where the addition of 5% water was not included in the gas feed, was also assessed using the different CeO_2 catalysts (Figure S1). The activity trends shown for propane oxidation under dry conditions mirror those under wet conditions, with the CeO_2 (IV) catalyst remaining by far the most active. However, conversion to CO_2 was slightly increased for both catalysts under dry conditions indicating the inclusion of 5% water to the gas feed slightly inhibited propane oxidation. Marécot et al. reported that the addition of water inhibited propane and propene oxidation over Pt and Pd catalysts due to a decrease in the number of active surface sites [44]. Furthermore, researchers have previously reported the addition of water negatively impacted propane oxidation over metal oxide catalysts, which was thought to occur from competitive adsorption between water and propane on the catalyst surface [5,45]. Water inhibition has also been observed for other VOCs, such as toluene [2]. It was proposed that the addition of water created competition for adsorption sites with the VOC, leading to surface active sites being blocked by water [46,47]. Our current data and these other studies emphasise the importance of considering water in the VOC effluent.

It is shown from XRD and Raman characterisation that both catalysts had the common cubic fluorite CeO_2 structure. In addition, the lattice parameter, crystallite size and bulk defect concentration calculated using these techniques were very similar for both catalysts. Furthermore, whilst differences in large-scale morphology were identified by TEM and

SEM, the small-scale morphology for both catalysts were similar, with the (111) lattice plane exposed preferentially for both catalysts.

The redox properties of CeO_2 catalysts are thought to be important for oxidation reactions that occur via a Mars-van Krevelen mechanism, often showing a relationship between activity and increased H_2 consumption and more facile reducibility [48]. The ability to easily remove active oxygen from the catalyst surface facilitates C-H bond activation, which is known to be the rate determining step for propane oxidation [49]. From the data shown (Figure 11), the catalytic activity is greater for the CeO_2 (IV) catalyst. This suggests that the slightly enhanced redox behaviour of the CeO_2 (III) catalyst is less significant for controlling activity, and the surface areas of the catalysts are a far more important parameter.

From the TPR-TPO cycles carried out, it was shown that the surface H_2 consumption significantly decreased, roughly ten-fold, for the CeO_2 (III) catalyst in the second cycle, compared with CeO_2 (IV). The H_2 consumption of the second cycle was more comparable between the two catalysts, with CeO_2 (III) having only a slightly increased value. As previously mentioned, this suggests that the initial TPR may not be representative of the redox properties of the catalyst under reaction conditions.

The surface areas resulting from the different catalyst precursors are considered to be very influential when understanding the catalytic activity. It has been well documented by various researchers that the high surface area of CeO_2 is a key factor for improved catalytic activity of aromatic VOC oxidation such as naphthalene oxidation [14,50,51]. Similar conclusions can be drawn from the data presented in Figure 11, as the high surface area CeO_2 (IV) catalyst was more active for propane total oxidation. Previous research has also shown increased surface area of metal oxide catalysts improved the catalytic activity of propane oxidation due to the increased amount of active sites available [52,53]. When normalised for surface area, both catalysts have similar activity showing a linear relationship between catalytic activity and surface area, indicating this factor to be the most influential when understanding catalyst activity.

The identification of surface oxygen defect sites by XPS analysis showed that the CeO_2 (IV) catalyst contained a higher proportion of these sites compared to the CeO_2 (III) catalyst. Previous research using the same preparation precursor has indicated a strong correlation between the increased amount of surface oxygen defect sites and improved catalytic activity for propane oxidation [12]. However, the influence of catalyst precursor in this study identifies the varying surface areas as the most influential factor when determining catalytic activity.

As mentioned previously, Na is known to be a poison of metal oxide catalysts for certain oxidation reactions [43]. This factor is particularly important when considering catalytic activity for the total oxidation of propane, as Tang et al. demonstrated that Na greatly hinders this process [54]. It was proposed that Na negatively impacts oxygen mobility by supressing oxygen desorption at lower temperatures, in addition to accumulating high amounts of surface carbonate species at higher temperatures. The impact of poor oxygen mobility from Na poisoning is consistent with extended studies for the oxidation of propane [55]. The impact of increased Na content on the catalyst surface did not impact the oxidation of propane in this work.

The most important factor influencing propane total oxidation activity was the catalyst surface areas, as a relationship can be concluded from data presented in Table 4. Hence, it is important to highlight the influence that the catalyst precursor has on the final catalyst, as a relatively subtle change of the cerium precursor oxidation state is significant. As shown from TGA-DTA and XRD analysis, the use of different precursors results in different precipitation products which, on calcination, form cubic fluorite CeO_2 with subtle differences that are important for catalytic performance.

The formation of a $CeO_2.nH_2O$ precipitate greatly increases the surface area of the resulting catalyst as evidenced by the CeO_2 (IV) catalyst. This effect has also been shown in previous research for the synthesis of Sm-doped CeO_2 mixed oxide catalysts [56]. Fur-

thermore, studies comparing either the cerium precursor or precipitating agent have drawn similar conclusions, with the Ce^{IV} precursor or the $CeO_2.H_2O$ precipitate resulting in the highest surface area [24,57]. Transformation of the $CeO_2.H_2O$ precipitate to the CeO_2 catalyst is likely to be topotactic, with very little alteration to the crystal structure from the removal of H_2O or ^{-}OH species. In contrast, the structure of the orthorhombic $Ce_2(OH)_2(CO_3)_2.H_2O$ precipitate differs significantly from the cubic fluorite structure of CeO_2, and decomposition occurs via an intermediate oxycarbonate species [30,58]. This disruptive decomposition phase transformation mechanism will result in the decreased surface area shown by the CeO_2 (III) catalyst. Furthermore, the $Ce_2(OH)_2(CO_3)_2.H_2O$ precipitate contains cerium in the Ce^{3+} oxidation state, requiring an oxidation step to produce the CeO_2 catalyst. Spiridigliozzi et al. found that under hydrothermal conditions, the initially formed metastable $Ce(OH)(CO_3)$ precipitate undergoes structural changes, as well as oxidation in solution after a long period of time [59]. However, the decomposition of the $Ce(OH)(CO_3)$ precipitate by heat treatment also induces the oxidation of the Ce^{3+} species to Ce^{4+}. It is stated that the thermal decomposition of the $Ce(OH)(CO_3).H_2O$ species results in a combination of endothermic decomposition from dehydration and carbonate decomposition, in addition to an exothermic reaction from the oxidation of Ce^{3+} to Ce^{4+} [30]. This exothermic reaction could increase the driving force to form the thermodynamically stable CeO_2 structure with the increased Ce^{4+} surface concentration observed for the lower activity CeO_2 (III) catalyst.

3. Materials and Methods

3.1. Catalyst Preparation

Two CeO_2 catalysts were prepared by a precipitation method, utilising a Metrohm 902 Titrando auto-titrator (Metrohm, Cheshire, UK). Aqueous $(NH_4)_2Ce(NO_3)_6$ (Acros Organics, Geel, Belgium) and $Ce(NO_3)_3$ (Merck, Gillingham, UK) were used as Ce^{IV} and Ce^{III} sources respectively, with aqueous Na_2CO_3 (Merck, Gillingham, UK) as the precipitating agent. In a typical synthesis, 100 mL of nitrate solution (0.25 M) and a solution of Na_2CO_3 (1 M) were added simultaneously to a thermostatically water heated jacketed vessel (80 °C). Addition rate of the nitrate solution was maintained constant (2 mL min^{-1}), whilst addition of Na_2CO_3 solution was automatically computer controlled to maintain a constant pH of 9. The precipitate formed was held at 80 °C for 1 h before being collected by vacuum filtration and washed with 2 L of hot deionised water.

The precipitates were dried at 110 °C for 16 h. Dried catalyst precipitates prior to calcination were denoted as d-CeO_2 (IV) and d-CeO_2 (III). Samples denoted as CeO_2 (IV) and CeO_2 (III) were the final catalysts prepared by calcination of the precipitates in static air at 500 °C for 3 h, with a ramp rate of 5 °C min^{-1}.

3.2. Catalyst Characterisation

Thermal gravimetric analysis (TGA) and differential thermal analysis (DTA) were performed using a Setaram Labsys 1600 instrument (SCIMED, Cheshire, UK). Approximately 30 mg of sample was loaded into an alumina crucible and heated to 700 °C at a rate of 5 °C min^{-1} in a flow of synthetic air (50 mL min^{-1}). For all TGA-DTA analysis, blank runs were subtracted from the relevant data to account for any buoyancy effects.

Powder X-ray diffraction (XRD) patterns were collected using a Panalytical X'Pert diffractometer (Malvern Panalytical, Worcestershire, UK) equipped with a Cu X-ray source operating at 40 kV and 40 mA. Analysis was carried out between 2θ values of 5–80°. Phase identification was achieved by matching patterns against the ICDD standard database. Application of the Scherrer equation was used to estimate crystallite size, comparing the experimental line widths of the four most dominant reflections ((111), (200), (220), (311)) against a highly crystalline silicon standard. An average crystallite size was then determined, with the (111) diffraction peak used to calculate lattice parameters.

A Quantachrome Quadrasorb Evo Analyser (Quantachrome, Hook, UK) was used for surface area analysis. Prior to analysis, catalysts were degassed under vacuum for 16 h at

120 °C. Surface areas of the catalysts were determined from twenty-point N_2 adsorption–desorption isotherms measured at −196 °C. The Brunauer–Emmett–Teller (BET) method was used to treat the data.

Raman spectra were obtained using a Renishaw inVia confocal Raman microscope (Renishaw, Gloucestershire, UK) with an Ar^+ visible green laser (514 nm). Spectra were collected in a reflective mode from samples mounted on a steel holder by a highly sensitive charge couple device (CCD) detector. The defect ratio (A_{590}/A_{463}) was calculated using the area of the bands at 590 cm^{-1} and 463 cm^{-1}.

Temperature programmed reduction and oxidation (TPR, TPO) were performed using a Quantachrome ChemBET (Quantachrome, Hook, UK). Pre-treatment of catalysts were carried out under a flow of He for 1 h at 120 °C. Reduction profiles were obtained by analysing approximately 50 mg of catalyst under a flow of 10% H_2/Ar (50 mL min^{-1}), over the temperature range 50–700 °C, with a heating rate of 10 °C min^{-1}. H_2 consumption was calculated by calibration against a CuO standard.

TPR-TPO cycles were run using the same conditions stated above. Once the initial TPR was completed, the catalyst sample was cooled under flowing He. TPO profiles were then attained under a flow of 10% O_2/He (50 mL min^{-1}), over the temperature range 50–700 °C, with a heating rate of 10 °C min^{-1}. Subsequently, a second TPR was completed.

A Kratos Axis Ultra DLD system (Kratos Analytical, Manchester, UK) was used for X-ray photoelectron spectroscopy (XPS). Spectra were collected using a monochromatic Al Kα X-ray source operating at 140 W (10 mA and 14 kV). Pass energies of 160 eV for survey spectra and 20 eV for the high-resolution scans were employed for data collection, with step sizes of 1 eV and 0.1 eV respectively. The system was operated in the Hybrid mode, utilising both magnetic immersion and electrostatic lenses for high sensitivity. Spectra were acquired using the 'slot' aperture which defines an analysis area of approximately 700 × 300 μm^2. Sample surface charging was minimised by a magnetically confined low energy electron charge compensation system, with all spectra taken at a 90° angle. A base pressure of ca. 1×10^{-9} Torr was maintained during data collection. Data was calibrated to the C 1s line of adventitious carbon (248.8 eV) and analysed using CasaXPS v2.3.24 [60] after subtraction of a Shirley background and using modified Wagner sensitivity factors, which take in to account the electron escape depth, as supplied by the manufacturer. Peak fits were performed using Voigt type functions and where applicable, modelled on line shapes derived from bulk standards, such as stoichiometric CeO_2.

Scanning Electron Microscopy (SEM) was obtained from a Tescan MAIA3 field emission gun scanning electron microscope (Tescan, Cambridge, UK) (FEG-SEM) with secondary and backscattered electron detectors. Energy-dispersive X-ray (EDX) analysis was performed using an Oxford Instruments $XMax^N$ 80 detector (Oxford Instruments, Abingdon, UK). The Point and ID function on the Oxford Aztec software was used to perform EDX analysis. Catalysts loaded onto carbon tape were sputter coated with 15 nm Au/Pd to prevent charging. A minimum of three areas were analysed across multiple particles and averaged to produce atomic %.

Transmission electron microscopy (TEM) was performed using a JEOL JEM 2100 (JEOL UK, Welwyn Garden City, UK) operating at 200 kV. Samples were prepared by dry dispersion over a 300 mesh copper grid coated with holey carbon film.

3.3. Catalyst Testing

Catalyst performance for the total oxidation of propane was assessed using a continuous flow fixed bed microreactor. A constant volume of catalyst was secured in a $\frac{1}{4}$ inch stainless steel tube between two plugs of quartz wool. A premixed cylinder of 5000 ppm propane in air was used, with the gas flow regulated at 50 mL min^{-1} by electronic mass flow controllers. A water saturator was attached and held at constant temperature to produce a 5% water saturation in the gas feed. A constant powdered catalyst volume of 0.067 mL was used, resulting in a catalyst mass of approximately 0.1 g and 0.3 g for CeO_2 (III) and CeO_2 (IV) respectively, to give a gas hourly space velocity (GHSV) of 45,000 h^{-1}.

The temperature range 200–600 °C was used to measure catalyst activity, with the temperature maintained and controlled by a K-type thermocouple placed into the catalyst bed. The reactor temperature was increased incrementally and allowed to stabilise until steady state was attained at each temperature before analysing the reactor effluent. The reaction effluent was analysed by an online gas chromatograph (Agilent 7890B) with two detectors in series (Agilent Technologies LDA UK Ltd., Stockport, Cheshire, UK). A thermal conductivity detector (TCD) was used to analyse O_2 and N_2. In addition, a flame ionisation detector (FID) equipped with a methaniser was used to analyse CO, CO_2, and hydrocarbons. Using HayeSep Q (80–100 mesh, 1.8 m × 3.2 mm) and MolSieve 13 X (80–100 mesh, 2 m × 3.2 mm) packed columns, with a series/by-pass valving configuration, separation was achieved. Analyses were performed at each temperature until three consistent sets of analytical data were obtained, indicating steady-state operation. Propane conversion was calculated by comparing the measured counts at each temperature to the blank analysis before each test.

4. Conclusions

CeO_2 catalysts were prepared by a precipitation method using either Ce^{III} or Ce^{IV} nitrate precursors to determine the influence on the catalytic activity for propane total oxidation. The CeO_2 catalyst prepared using the Ce^{IV} precursor had improved performance for propane total oxidation. The catalytic activity was related to the formation of different precipitated species during synthesis of the catalyst precursor and their transformation to the CeO_2 catalyst. Formation of $CeO_2.nH_2O$ from the Ce^{IV} precursor salt resulted in a higher surface area catalyst with increased concentration of surface oxygen defect sites and reduced cerium species. Formation of the $Ce_2(OH)_2(CO_3)_2.H_2O$ precipitate from the Ce^{III} precursor salt resulted in slightly improved redox properties but had a very low surface area. A direct relationship between catalyst surface area and catalytic activity was found to be the most influential factor for the total oxidation of propane.

Supplementary Materials: The following are available online at https://www.mdpi.com/article/10.3390/catal11121461/s1, Figure S1: Catalyst activity for propane total oxidation under wet and dry conditions.

Author Contributions: Conceptualization, S.H.T.; Data curation, K.A., T.E.D., D.J.M. and D.H.; Formal analysis, K.A., T.E.D., D.J.M. and D.H.; Methodology, K.A.; Supervision, S.H.T.; Writing—review and editing, K.A., T.E.D., D.J.M. and S.H.T. All authors have read and agreed to the published version of the manuscript.

Funding: This research received no external funding.

Data Availability Statement: Data is contained within the article.

Acknowledgments: The authors acknowledge financial support from Cardiff University.

Conflicts of Interest: The authors declare no conflict of interest.

References

1. Wuebbles, D.J.; Sanyal, S. Air Quality in a Cleaner Energy World. *Curr. Pollut. Rep.* **2015**, *1*, 117–129. [CrossRef]
2. He, C.; Cheng, J.; Zhang, X.; Douthwaite, M.; Pattisson, S.; Hao, Z. Recent Advances in the Catalytic Oxidation of Volatile Organic Compounds: A Review Based on Pollutant Sorts and Sources. *Chem. Rev.* **2019**, *119*, 4471–4568. [CrossRef]
3. Wang, P.; Cui, C.; Li, K.; Yi, J.; Lei, L. The Effect of Mn Content on Catalytic Activity of the Co–Mn–Ce Catalysts for Propane Oxidation: Importance of Lattice Defect and Surface Active Species. *Catal. Lett.* **2020**, *150*, 1505–1514. [CrossRef]
4. Choudhary, V.R.; Deshmukh, G.M.; Mishra, D.P. Kinetics of the Complete Combustion of Dilute Propane and Toluene over Iron-Doped ZrO2 Catalyst. *Energy Fuels* **2005**, *19*, 54–63. [CrossRef]
5. Zhang, C.; Zeng, K.; Wang, C.; Liu, X.; Wu, G.; Wang, Z.; Wang, D. $LaMnO_3$ Perovskites via a Facile Nickel Substitution Strategy for Boosting Propane Combustion Performance. *Ceram. Int.* **2020**, *46*, 6652–6662. [CrossRef]
6. Hu, Z.; Qiu, S.; You, Y.; Guo, Y.; Guo, Y.; Wang, L.; Zhan, W.; Lu, G. Hydrothermal Synthesis of NiCeOx Nanosheets and Its Application to the Total Oxidation of Propane. *Appl. Catal. B Environ.* **2018**, *225*, 110–120. [CrossRef]
7. Xiao, Y.; Zhao, W.; Zhang, K.; Zhang, Y.; Wang, X.; Zhang, T.; Wu, X.; Chen, C.; Jiang, L. Facile Synthesis of Mn–Fe/CeO2 Nanotubes by Gradient Electrospinning and Their Excellent Catalytic Performance for Propane and Methane Oxidation. *Dalton Trans.* **2017**, *46*, 16967–16972. [CrossRef]

8. Yang, C.; Miao, G.; Pi, Y.; Xia, Q.; Wu, J.; Li, Z.; Xiao, J. Abatement of Various Types of VOCs by Adsorption/Catalytic Oxidation: A Review. *Chem. Eng. J.* **2019**, *370*, 1128–1153. [CrossRef]
9. Krishnamurthy, A.; Adebayo, B.; Gelles, T.; Rownaghi, A.; Rezaei, F. Abatement of Gaseous Volatile Organic Compounds: A Process Perspective. *Catal. Today* **2020**, *350*, 100–119. [CrossRef]
10. Taylor, M.; Ndifor, E.N.; Garcia, T.; Solsona, B.; Carley, A.F.; Taylor, S.H. Deep Oxidation of Propane Using Palladium–Titania Catalysts Modified by Niobium. *Appl. Catal. Gen.* **2008**, *350*, 63–70. [CrossRef]
11. Shah, P.M.; Burnett, J.W.H.; Morgan, D.J.; Davies, T.E.; Taylor, S.H. Ceria–Zirconia Mixed Metal Oxides Prepared via Mechanochemical Grinding of Carbonates for the Total Oxidation of Propane and Naphthalene. *Catalysts* **2019**, *9*, 475. [CrossRef]
12. Shah, P.M.; Day, A.N.; Davies, T.E.; Morgan, D.J.; Taylor, S.H. Mechanochemical Preparation of Ceria-Zirconia Catalysts for the Total Oxidation of Propane and Naphthalene Volatile Organic Compounds. *Appl. Catal. B Environ.* **2019**, *253*, 331–340. [CrossRef]
13. Montini, T.; Melchionna, M.; Monai, M.; Fornasiero, P. Fundamentals and Catalytic Applications of CeO2-Based Materials. *Chem. Rev.* **2016**, *116*, 5987–6041. [CrossRef] [PubMed]
14. Garcia, T.; Solsona, B.; Taylor, S.H. Nano-Crystalline Ceria Catalysts for the Abatement of Polycyclic Aromatic Hydrocarbons. *Catal. Lett.* **2005**, *105*, 183–189. [CrossRef]
15. Setiabudi, A.; Chen, J.; Mul, G.; Makkee, M.; Moulijn, J.A. CeO2 Catalysed Soot Oxidation: The Role of Active Oxygen to Accelerate the Oxidation Conversion. *Appl. Catal. B Environ.* **2004**, *51*, 9–19. [CrossRef]
16. Zheng, X.; Li, Y.; Zhang, L.; Shen, L.; Xiao, Y.; Zhang, Y.; Au, C.; Jiang, L. Insight into the Effect of Morphology on Catalytic Performance of Porous CeO2 Nanocrystals for H2S Selective Oxidation. *Appl. Catal. B Environ.* **2019**, *252*, 98–110. [CrossRef]
17. Krishna, K.; Bueno-López, A.; Makkee, M.; Moulijn, J.A. Potential Rare Earth Modified CeO2 Catalysts for Soot Oxidation: I. Characterisation and Catalytic Activity with O2. *Appl. Catal. B Environ.* **2007**, *75*, 189–200. [CrossRef]
18. Wang, Z.; Shen, G.; Li, J.; Liu, H.; Wang, Q.; Chen, Y. Catalytic Removal of Benzene over CeO2–MnOx Composite Oxides Prepared by Hydrothermal Method. *Appl. Catal. B Environ.* **2013**, *138–139*, 253–259. [CrossRef]
19. Lykaki, M.; Pachatouridou, E.; Carabineiro, S.A.C.; Iliopoulou, E.; Andriopoulou, C.; Kallithrakas-Kontos, N.; Boghosian, S.; Konsolakis, M. Ceria Nanoparticles Shape Effects on the Structural Defects and Surface Chemistry: Implications in CO Oxidation by Cu/CeO2 Catalysts. *Appl. Catal. B Environ.* **2018**, *230*, 18–28. [CrossRef]
20. Datta, S.; Torrente-Murciano, L. Nanostructured Faceted Ceria as Oxidation Catalyst. *Curr. Opin. Chem. Eng.* **2018**, *20*, 99–106. [CrossRef]
21. Torrente-Murciano, L.; Gilbank, A.; Puertolas, B.; Garcia, T.; Solsona, B.; Chadwick, D. Shape-Dependency Activity of Nanostructured CeO2 in the Total Oxidation of Polycyclic Aromatic Hydrocarbons. *Appl. Catal. B Environ.* **2013**, *132–133*, 116–122. [CrossRef]
22. Luo, L.; LaCoste, J.D.; Khamidullina, N.G.; Fox, E.; Gang, D.D.; Hernandez, R.; Yan, H. Investigate Interactions of Water with Mesoporous Ceria Using in Situ VT-DRIFTS. *Surf. Sci.* **2020**, *691*, 121486. [CrossRef]
23. Kurian, M.; Kunjachan, C. Investigation of Size Dependency on Lattice Strain of Nanoceria Particles Synthesised by Wet Chemical Methods. *Int. Nano Lett.* **2014**, *4*, 73–80. [CrossRef]
24. Qi, L.; Yu, Q.; Dai, Y.; Tang, C.; Liu, L.; Zhang, H.; Gao, F.; Dong, L.; Chen, Y. Influence of Cerium Precursors on the Structure and Reducibility of Mesoporous CuO-CeO2 Catalysts for CO Oxidation. *Appl. Catal. B Environ.* **2012**, *119–120*, 308–320. [CrossRef]
25. Zhang, C.; Chu, W.; Chen, F.; Li, L.; Jiang, R.; Yan, J. Effects of Cerium Precursors on Surface Properties of Mesoporous CeMnOx Catalysts for Toluene Combustion. *J. Rare Earths* **2020**, *38*, 70–75. [CrossRef]
26. Guillén-Hurtado, N.; Atribak, I.; Bueno-López, A.; García-García, A. Influence of the Cerium Precursor on the Physico-Chemical Features and NO to NO2 Oxidation Activity of Ceria and Ceria–Zirconia Catalysts. *J. Mol. Catal. Chem.* **2010**, *323*, 52–58. [CrossRef]
27. Sellick, D.R.; Aranda, A.; García, T.; López, J.M.; Solsona, B.; Mastral, A.M.; Morgan, D.J.; Carley, A.F.; Taylor, S.H. Influence of the Preparation Method on the Activity of Ceria Zirconia Mixed Oxides for Naphthalene Total Oxidation. *Appl. Catal. B Environ.* **2013**, *132–133*, 98–106. [CrossRef]
28. D'Assunção, L.M.; Giolito, I.; Ionashiro, M. Thermal Decomposition of the Hydrated Basic Carbonates of Lanthanides and Yttrium. *Thermochim. Acta* **1989**, *137*, 319–330. [CrossRef]
29. Padeste, C.; Cant, N.W.; Trimm, D.L. Thermal Decomposition of Pure and Rhodium Impregnated Cerium(III) Carbonate Hydrate in Different Atmospheres. *Catal. Lett.* **1994**, *24*, 95–105. [CrossRef]
30. Wakita, H.; Kinoshita, S. A Synthetic Study of the Solid Solutions in the Systems and La2(CH3)3·8H2O-Ce2(CO3)3·8H2O and La(OH)CO3–Ce(OH)CO3. *Bull. Chem. Soc. Jpn.* **1979**, *52*, 428–432. [CrossRef]
31. Hirano, M.; Kato, E. Hydrothermal Synthesis of Two Types of Cerium Carbonate Particles. *J. Mater. Sci. Lett.* **1999**, *18*, 403–405. [CrossRef]
32. Hirano, M.; Kato, E. Hydrothermal Synthesis of Nanocrystalline Cerium(IV) Oxide Powders. *J. Am. Ceram. Soc.* **1999**, *82*, 786–788. [CrossRef]
33. Pettinger, N.W.; Williams, R.E.A.; Chen, J.; Kohler, B. Crystallization Kinetics of Cerium Oxide Nanoparticles Formed by Spontaneous, Room-Temperature Hydrolysis of Cerium(IV) Ammonium Nitrate in Light and Heavy Water. *Phys. Chem. Chem. Phys.* **2017**, *19*, 3523–3531. [CrossRef]
34. Lowell, S.; Shields, J.E.; Thomas, M.A.; Thommes, M. *Characterization of Porous Solids and Powders: Surface Area, Pore Size and Density*; Springer Science & Business Media, 2012; ISBN 978-1-4020-2303-3.

35. Thommes, M.; Kaneko, K.; Neimark, A.V.; Olivier, J.P.; Rodriguez-Reinoso, F.; Rouquerol, J.; Sing, K.S.W. Physisorption of Gases, with Special Reference to the Evaluation of Surface Area and Pore Size Distribution (IUPAC Technical Report). *Pure Appl. Chem.* **2015**, *87*, 1051–1069. [CrossRef]
36. Wu, Z.; Li, M.; Howe, J.; Meyer, H.M.; Overbury, S.H. Probing Defect Sites on CeO2 Nanocrystals with Well-Defined Surface Planes by Raman Spectroscopy and O2 Adsorption. *Langmuir* **2010**, *26*, 16595–16606. [CrossRef] [PubMed]
37. López, J.M.; Gilbank, A.L.; García, T.; Solsona, B.; Agouram, S.; Torrente-Murciano, L. The Prevalence of Surface Oxygen Vacancies over the Mobility of Bulk Oxygen in Nanostructured Ceria for the Total Toluene Oxidation. *Appl. Catal. B Environ.* **2015**, *174–175*, 403–412. [CrossRef]
38. Wang, Q.; Yeung, K.L.; Bañares, M.A. Ceria and Its Related Materials for VOC Catalytic Combustion: A Review. *Catal. Today* **2020**, *356*, 141–154. [CrossRef]
39. Zhang, F.; Wang, P.; Koberstein, J.; Khalid, S.; Chan, S.-W. Cerium Oxidation State in Ceria Nanoparticles Studied with X-Ray Photoelectron Spectroscopy and Absorption near Edge Spectroscopy. *Surf. Sci.* **2004**, *563*, 74–82. [CrossRef]
40. Trovarelli, A.; Llorca, J. Ceria Catalysts at Nanoscale: How Do Crystal Shapes Shape Catalysis? *ACS Catal.* **2017**, *7*, 4716–4735. [CrossRef]
41. Wang, K.; Chang, Y.; Lv, L.; Long, Y. Effect of Annealing Temperature on Oxygen Vacancy Concentrations of Nanocrystalline CeO2 Film. *Appl. Surf. Sci.* **2015**, *351*, 164–168. [CrossRef]
42. Holgado, J.P.; Munuera, G.; Espinós, J.P.; González-Elipe, A.R. XPS Study of Oxidation Processes of CeOx Defective Layers. *Appl. Surf. Sci.* **2000**, *158*, 164–171. [CrossRef]
43. Mirzaei, A.A.; Shaterian, H.R.; Joyner, R.W.; Stockenhuber, M.; Taylor, S.H.; Hutchings, G.J. Ambient Temperature Carbon Monoxide Oxidation Using Copper Manganese Oxide Catalysts: Effect of Residual Na+ Acting as Catalyst Poison. *Catal. Commun.* **2003**, *4*, 17–20. [CrossRef]
44. Marécot, P.; Fakche, A.; Kellali, B.; Mabilon, G.; Prigent, P.; Barbier, J. Propane and Propene Oxidation over Platinum and Palladium on Alumina: Effects of Chloride and Water. *Appl. Catal. B Environ.* **1994**, *3*, 283–294. [CrossRef]
45. Zhu, W.; Chen, X.; Jin, J.; Di, X.; Liang, C.; Liu, Z. Insight into Catalytic Properties of Co3O4-CeO2 Binary Oxides for Propane Total Oxidation. *Chin. J. Catal.* **2020**, *41*, 679–690. [CrossRef]
46. Xia, Y.; Xia, L.; Liu, Y.; Yang, T.; Deng, J.; Dai, H. Concurrent Catalytic Removal of Typical Volatile Organic Compound Mixtures over Au-Pd/α-MnO2 Nanotubes. *J. Environ. Sci.* **2018**, *64*, 276–288. [CrossRef]
47. Fang, J.; Chen, X.; Xia, Q.; Xi, H.; Li, Z. Effect of Relative Humidity on Catalytic Combustion of Toluene over Copper Based Catalysts with Different Supports. *Chin. J. Chem. Eng.* **2009**, *17*, 767–772. [CrossRef]
48. García, T.; Solsona, B.; Taylor, S.H. Naphthalene Total Oxidation over Metal Oxide Catalysts. *Appl. Catal. B Environ.* **2006**, *66*, 92–99. [CrossRef]
49. Luo, J.-Y.; Meng, M.; Yao, J.-S.; Li, X.-G.; Zha, Y.-Q.; Wang, X.; Zhang, T.-Y. One-Step Synthesis of Nanostructured Pd-Doped Mixed Oxides MOx-CeO2 (M=Mn, Fe, Co, Ni, Cu) for Efficient CO and C3H8 Total Oxidation. *Appl. Catal. B Environ.* **2009**, *87*, 92–103. [CrossRef]
50. Aranda, A.; Puértolas, B.; Solsona, B.; Agouram, S.; Murillo, R.; Mastral, A.M.; Taylor, S.H.; Garcia, T. Total Oxidation of Naphthalene Using Mesoporous CeO2 Catalysts Synthesized by Nanocasting from Two Dimensional SBA-15 and Three Dimensional KIT-6 and MCM-48 Silica Templates. *Catal. Lett.* **2010**, *134*, 110–117. [CrossRef]
51. Ndifor, E.N.; Garcia, T.; Solsona, B.; Taylor, S.H. Influence of Preparation Conditions of Nano-Crystalline Ceria Catalysts on the Total Oxidation of Naphthalene, a Model Polycyclic Aromatic Hydrocarbon. *Appl. Catal. B Environ.* **2007**, *76*, 248–256. [CrossRef]
52. Solsona, B.; Garcia, T.; Aylón, E.; Dejoz, A.M.; Vázquez, I.; Agouram, S.; Davies, T.E.; Taylor, S.H. Promoting the Activity and Selectivity of High Surface Area Ni–Ce–O Mixed Oxides by Gold Deposition for VOC Catalytic Combustion. *Chem. Eng. J.* **2011**, *175*, 271–278. [CrossRef]
53. Garcia, T.; Agouram, S.; Sánchez-Royo, J.F.; Murillo, R.; Mastral, A.M.; Aranda, A.; Vázquez, I.; Dejoz, A.; Solsona, B. Deep Oxidation of Volatile Organic Compounds Using Ordered Cobalt Oxides Prepared by a Nanocasting Route. *Appl. Catal. Gen.* **2010**, *386*, 16–27. [CrossRef]
54. Tang, W.; Weng, J.; Lu, X.; Wen, L.; Suburamanian, A.; Nam, C.-Y.; Gao, P.-X. Alkali-Metal Poisoning Effect of Total CO and Propane Oxidation over Co3O4 Nanocatalysts. *Appl. Catal. B Environ.* **2019**, *256*, 117859. [CrossRef]
55. Chai, G.; Zhang, W.; Guo, Y.; Valverde, J.L.; Giroir-Fendler, A. The Influence of Residual Sodium on the Catalytic Oxidation of Propane and Toluene over Co3O4 Catalysts. *Catalysts* **2020**, *10*, 867. [CrossRef]
56. Spiridigliozzi, L.; Dell'Agli, G.; Biesuz, M.; Sglavo, V.M.; Pansini, M. Effect of the Precipitating Agent on the Synthesis and Sintering Behavior of 20 Mol Sm-Doped Ceria. *Adv. Mater. Sci. Eng.* **2016**. [CrossRef]
57. Wang, L.; Liu, H.; Liu, Y.; Chen, Y.; Yang, S. Effect of Precipitants on Ni-CeO2 Catalysts Prepared by a Co-Precipitation Method for the Reverse Water-Gas Shift Reaction. *J. Rare Earths* **2013**, *31*, 969–974. [CrossRef]
58. Li, J.-G.; Ikegami, T.; Wang, Y.; Mori, T. Reactive Ceria Nanopowders via Carbonate Precipitation. *J. Am. Ceram. Soc.* **2002**, *85*, 2376–2378. [CrossRef]

59. Spiridigliozzi, L.; Accardo, G.; Frattini, D.; Marocco, A.; Esposito, S.; Freyria, F.S.; Pansini, M.; Dell'Agli, G. Effect of RE3+ on Structural Evolution of Rare-Earth Carbonates Synthesized by Facile Hydrothermal Treatment. *Adv. Mater. Sci. Eng.* **2019**, *2019*, e1241056. [CrossRef]
60. Fairley, N.; Fernandez, V.; Richard-Plouet, M.; Guillot-Deudon, C.; Walton, J.; Smith, E.; Flahaut, D.; Greiner, M.; Biesinger, M.; Tougaard, S.; et al. Systematic and Collaborative Approach to Problem Solving Using X-Ray Photoelectron Spectroscopy. *Appl. Surf. Sci. Adv.* **2021**, *5*, 100112. [CrossRef]